Statistical sources for broadband shock-associated noise using the Navier-Stokes equations

Trushant K. Patel[a] and Steven A. E. Miller
Department of Mechanical and Aerospace Engineering, University of Florida, P.O. Box 116250, Gainesville, Florida 32611, USA

(Received 11 May 2019; revised 28 October 2019; accepted 11 November 2019; published online 19 December 2019)

A decomposition of the Navier-Stokes equations is used to identify the equivalent source term for broadband shock-associated noise (BBSAN). An analytical closed-form model to predict BBSAN is developed using an acoustic analogy based on the Navier-Stokes equations. The field-variables are decomposed into the base flow, aerodynamic fluctuations, and acoustic fluctuations. The spectral densities of fluctuating acoustic quantities are obtained by convolving the vector Green's function with the source terms involving the two-point cross-correlation of the aerodynamic quantities. The scaling of the source term with the off-design parameter $\beta = (|M_j^2 - M_d^2|)^{1/2}$ is compared with experimental results. The base flow is obtained using a Reynolds-averaged Navier-Stokes solution, while the fluctuating statistical quantities are obtained using theoretical and experimental results. This paper identifies the equivalent source of BBSAN based on the scaling analysis and the physical mechanism of shock-associated noise. The identified source term resides within the Navier-Stokes equations without further rearrangement and correlates very highly with BBSAN. Predictions for BBSAN are made at multiple observer angles and nozzle pressure ratios using the identified source term, and these predictions compare favorably with the experimental results. Finally, identification of the source locations in the jet exhaust responsible for BBSAN at different Strouhal numbers is performed. https://doi.org/10.1121/1.5139216

[AA] Pages: 4339–4351

I. INTRODUCTION

Jet noise has been a major concern for over 70 years in military and commercial aviation and has a negative impact on residential areas. In military applications, jet noise creates adverse effects on the health and hearing of the military personnel working nearby an aircraft. Approximately 107 000 sailors are living and working aboard US Navy ships, and 800×10^6 dollars were spent for hearing loss as disability benefits of veterans in 2005.[1] Recently, disability benefits have risen to over a billion dollars annually. In order to maximize the thrust during take-off on short runways, the jet engines are often operated at under-expanded conditions. This creates a large pressure mismatch at the exit of the nozzle, resulting in a shock-cell structure within the jet exhaust. The large-scale turbulent structures in the shear layer interact with the shock-cell structure resulting in shock-associated noise. Figure 1 shows a picture of military personnel in close proximity to the aircraft during take-off. The shock-cells are observed within the exhaust of the jet engine in Fig. 1.

An off-design supersonic jet generates two types of noise, which are turbulent mixing noise and shock-associated noise. The turbulent mixing noise is the noise directly radiated from turbulent structures and can be categorized into large-scale coherent noise and fine-scale incoherent noise.[2] The shock-associated noise has two components as well, one with discrete frequencies, often known as "screech" tones,[3] while the other is a broadband component, known as broadband shock-associated noise (BBSAN). An excellent review paper on the different types of noise components and their characteristics is written by Tam.[4] A sample pressure spectrum located at 100 jet diameters from the nozzle exit in the sideline direction ($\theta = 90°$) is shown in Fig. 2. The experimental spectrum is from the small hot jet acoustic rig (SHJAR) database[5] from NASA Glenn Research Center at Lewis Field. The fine-scale mixing noise, which is relatively spatially incoherent, and the BBSAN are plotted using the empirical forms of Tam *et al.*[6] and Kuo *et al.*,[7] respectively. As large-scale mixing noise is dominant in the downstream direction, it is not plotted in Fig. 2. The fine-scale mixing noise and BBSAN are dominant in the sideline and upstream direction. This paper focuses on the identification of the shock-noise source term from Navier-Stokes equations and its subsequent prediction and analysis.

Harper-Bourne and Fisher[8] were the first to study and develop a semi-empirical model of BBSAN. Each shock-cell was considered to be an origin of the noise source for BBSAN. Noise from these sources interferes either constructively or destructively, depending on the phase speed of the large eddies. A stochastic model was developed by Tam[9] based on the theory and scaling of BBSAN with nozzle pressure ratios (NPR) and total temperature ratios (TTR), given by Tam and Tanna.[10] Tam and Chen[11] modeled instability waves from the large-scale structures separately, and superposed the instability waves with the shock-cell structure of imperfectly expanded supersonic jets[12] to create a model for BBSAN. Morris and Miller[13] developed an acoustic analogy based model for predicting the BBSAN based on linearized

[a]Electronic mail: trushant@ufl.edu

FIG. 1. (Color online) F/A-18C Hornet on USS Theodore Roosevelt. USN public release photo: 180123-N-GP724-1102.

Euler equations (LEE) and Reynolds-averaged Navier-Stokes (RANS) simulations. Suzuki[14] created a model to predict BBSAN using wave-packets and large-eddy simulation (LES). He created a semi-empirical model of the cross-correlation of the proper orthogonal decomposition modes of near-field LES data and used those to predict the sound pressure level (SPL) at different Strouhal numbers in the far-field.

Although the above prediction models yield excellent prediction results, the true source term responsible for BBSAN is not known. Harper-Bourne and Fisher[8] and Suzuki[14] use the cross-spectral correlation function of pressure at different shock-cell locations for prediction of BBSAN. The cross-correlation function used by Harper-Bourne and Fisher[8] is empirical in nature and based on the experimental scaling of shock-noise, while the one used by Suzuki[14] is a semi-empirical model based on a wave-packet model and LES data. Tam[9] used the method of matched asymptotic expansions to solve for pressure in the near- and far-field, and very little empiricism is present in his approach. The amplitude of pressure is approximated by an analytical model, and the spectral density of pressure is found by the Fourier transform of the auto-correlation of pressure. Morris and Miller[13] derived the source term for BBSAN using

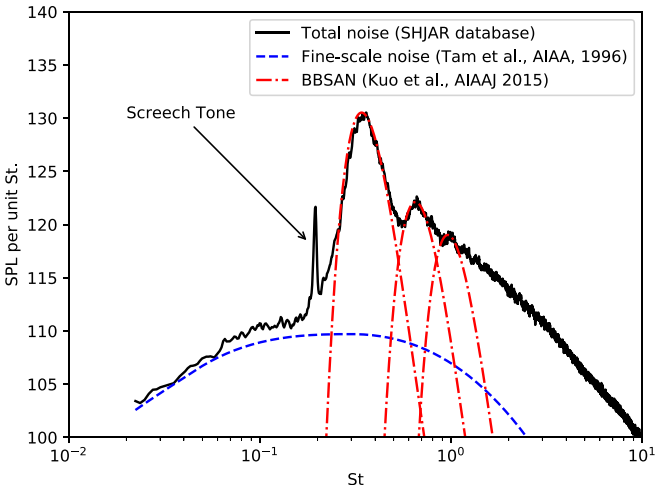

FIG. 2. (Color online) Jet noise spectrum with empirical source spectra in the sideline direction ($\theta = 90°$).

scaling or dimensional analysis of the unsteady force per unit volume associated with the interactions between the turbulent velocity fluctuations and the velocity perturbations associated with the shock-cells, which is the source term present on the right-hand side of the acoustic analogy based on LEE. In this paper, we identify the source terms for BBSAN using a newly formed acoustic analogy based on the decomposition of the Navier-Stokes equations.

To identify the source term for BBSAN, we perform an analysis of multiple terms obtained from the Navier-Stokes equations with varying NPRs. From their experiments, Harper-Bourne and Fisher[8] showed that the BBSAN scales as β^4. Here $\beta = (|M_j^2 - M_d^2|)^{1/2}$, where M_j is the fully-expanded jet Mach number while M_d is the design Mach number. Later, Tanna[15] and Tam and Tanna[10] confirmed the scaling of BBSAN as β^4 from their extensive experimental results. Various experiments by Seiner and Norum,[16,17] Norum and Seiner,[18–20] and Seiner and Yu[21] significantly enhanced our understanding of shock-associated noise. From theory, Tam[9] also confirmed the same scaling factor of β^4. Miller[22] also found that the source term in the Morris and Miller[13] model scales as β^4 for unheated jets. Kandula[23] proposed a theory based on the linear interaction of shock waves and vorticity and found that the intensity of BBSAN scales as $\beta^{4.2}$. Viswanathan *et al.*[24] found that the scaling of BBSAN varies from $\beta^{2.7}$ to $\beta^{6.17}$ depending on the observer angle as well as the TTR. However, for unheated jets in the sideline direction the scaling is close to β^4.

Various studies have been conducted to ascertain the source location of BBSAN. Norum and Seiner[18,19] and Seiner and Yu[21] found that the source locations for BBSAN are located near the end of the potential core, where the large-scale instability waves have reached maximum growth before breaking down. Seiner and Yu[21] identified the source locations of BBSAN using correlations from an array of near-field microphones. They show that the maximum noise comes from six to ten nozzle diameters downstream from the nozzle exit. Podboy *et al.*[25] used a phased microphone array with a beamforming method to find the source locations. They also found that the maximum noise radiates from the weak shocks at the end of the potential core region, where the shock-cell spacing is comparable to the length scale of the large-scale structures. Tan *et al.*[26] reconstructed the sources of BBSAN using the Morris and Miller[13] model. They used particle image velocimetry and RANS results as an input to the model and found that the sources are located within the first four to five shock-cells.

In order to reduce the intensity of BBSAN, we need to understand the source of the noise. The basis of our method is the newly developed acoustic analogy approach of Miller.[27] In the work of Miller,[27] an acoustic analogy was used to predict the noise from isotropic turbulence. However, as the analogy is based on the Navier-Stokes equations, it contains all the noise sources. In the present work, we try to identify the shock-noise source term from all the source terms present in the Navier-Stokes equations using this analogy.

The rest of the paper is organized as follows. The mathematical model of Miller[27] is discussed briefly in Sec. II A in the new context of shock-noise. Relevant arguments for the

model are derived in Secs. II B and II C. Identification of the source term for BBSAN is performed in Sec. II D, and the arguments are integrated into the model in Sec. II E. Predictions based on the newly developed model at different angles and with different NPRs are shown in Sec. III A, and source locations for BBSAN at different Strouhal numbers are shown in Sec. III B.

II. MATHEMATICAL MODEL

A. Navier-Stokes equations based acoustic analogy

A flow-chart for the acoustic analogy based on the decomposition of the Navier-Stokes equations is shown in Fig. 3. The field-variables in the Navier-Stokes equations are decomposed to time-averaged base flow, aerodynamic turbulent fluctuations, and the radiating acoustic fluctuations. The resulting equations are rearranged such that the radiating components are kept on the left-hand side, while the base flow and aerodynamic turbulent fluctuations are brought to the right-hand side. The left-hand side terms are linearized, and the spectral density of the radiating components is obtained by convolving the vector Green's function with the source terms present on the right-hand side.

Assuming that the fluid is in continuum and the Navier-Stokes equations govern the fluid flow, we write the continuity, momentum, and energy equation as

$$\frac{\partial \rho}{\partial t}+\frac{\partial \rho u_j}{\partial x_j}=0, \tag{1}$$

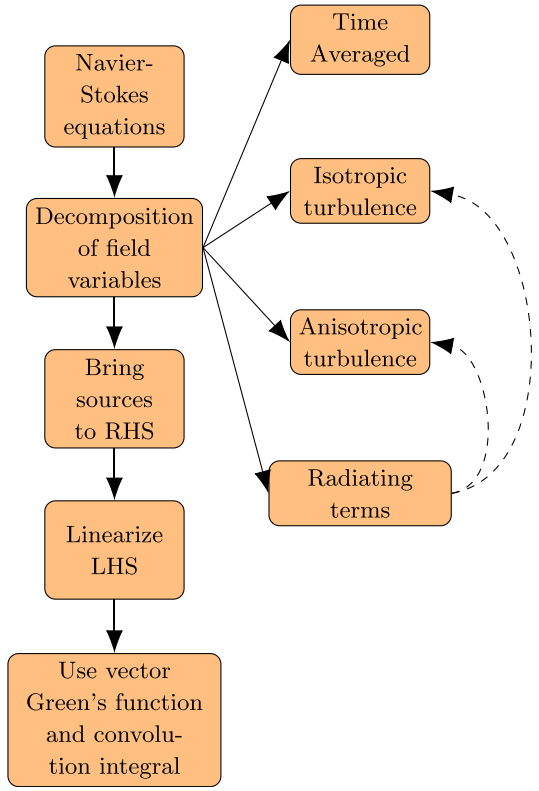

FIG. 3. (Color online) Flow-chart of the acoustic analogy based on the decomposition of the Navier-Stokes equations.

$$\frac{\partial \rho u_i}{\partial t}+\frac{\partial \rho u_i u_j}{\partial x_j}=-\frac{\partial p}{\partial x_j}\delta_{ij}+\frac{\partial}{\partial x_j}\left[\mu\left(\frac{\partial u_i}{\partial x_j}+\frac{\partial u_j}{\partial x_i}\right)\right]-\frac{2}{3}\frac{\partial}{\partial x_j}\left[\mu\frac{\partial u_k}{\partial x_k}\right], \tag{2}$$

and

$$\begin{aligned}\frac{\partial p}{\partial t}+\frac{\gamma-1}{2}\frac{\partial \rho u_k u_k}{\partial t}+\frac{\gamma-1}{2}\frac{\partial \rho u_j u_k u_k}{\partial x_j}&=-\gamma\frac{\partial u_j p}{\partial x_j}+(\gamma-1)\frac{\partial}{\partial x_j}\left[\frac{c_p\mu}{Pr}\frac{\partial T}{\partial x_j}\right]\\&+(\gamma-1)\frac{\partial}{\partial x_j}\left[\mu u_i\left(\frac{\partial u_i}{\partial x_j}+\frac{\partial u_j}{\partial x_i}\right)\right]\\&-(\gamma-1)\frac{2}{3}\delta_{ij}\frac{\partial}{\partial x_j}\left[\mu u_i\frac{\partial u_k}{\partial x_k}\right].\end{aligned} \tag{3}$$

Here, $\rho, \boldsymbol{u}, p$, and T represent the instantaneous density, velocity, pressure, and temperature of the fluid, respectively. The spatial position and time is denoted by $\boldsymbol{x}$ and t, respectively. Calorically perfect gas equations such as $p=\rho RT$, $e=c_vT$, $R=c_p-c_v$, and $\gamma=c_p/c_v$ are used for closure, where R is the universal gas constant, e is the internal energy, and c_p and c_v are the specific heats at constant pressure and volume, respectively. The Prandtl number is denoted by $Pr=c_p\mu/\lambda$, where μ is the dynamic viscosity and λ is the thermal conductivity. Kronecker delta function is represented by δ_{ij}. Note that the energy equation is converted to the pressure form using the calorically perfect gas equations, as we are interested in the pressure of the sound field at the observer location.

Miller[27] decomposes the field-variables such as pressure, velocity, temperature, etc., as

$$q=\bar{q}+\breve{q}+\hat{q}+q'+q'', \tag{4}$$

where q is any field-variable. The over-bar operator represents the time-averaged base flow. The breve operator indicates the fluctuations of spatially incoherent isotropic turbulence, while the hat operator indicates the fluctuations from coherent anisotropic turbulence. A single prime denotes the radiating component due to the anisotropic fluctuations, while a double prime denotes the radiating component due to the isotropic fluctuations. Justification of this approach is discussed by Miller.[27]

These decomposed field-variables are substituted in Eqs. (1)–(3). The resulting equations are rearranged such that the radiating terms are on the left-hand side of the equations, and the time-averaged base flow, isotropic fluctuations, and anisotropic fluctuations are brought to the right-hand side. The right-hand side of the equations results in the exact Navier-Stokes equations operating on the summation of base flow and turbulent fluctuations. The left-hand side terms are viewed as propagators, while the right-hand side terms of the equations are viewed as source terms. The source terms on the right-hand side can be written as

$$\Theta_0=-\frac{\partial \underline{\rho}}{\partial t}-\frac{\partial \underline{\rho u_j}}{\partial x_j}, \tag{5}$$

$$\Theta_i = -\frac{\partial \underline{\rho}\underline{u}_i}{\partial t} - \frac{\partial \underline{\rho}\underline{u}_i\underline{u}_j}{\partial x_j} - \frac{\partial \underline{p}}{\partial x_j}\delta_{ij} + \frac{\partial}{\partial x_j}\left[\mu\left(\frac{\partial \underline{u}_i}{\partial x_j} + \frac{\partial \underline{u}_j}{\partial x_i}\right)\right] - \frac{2}{3}\frac{\partial}{\partial x_j}\left[\mu\frac{\partial \underline{u}_k}{\partial x_k}\right], \tag{6}$$

and

$$\begin{aligned}\Theta_4 = &-\frac{\partial \underline{p}}{\partial t} - \frac{\gamma-1}{2}\frac{\partial \underline{\rho}\underline{u}_k\underline{u}_k}{\partial t} - \gamma\frac{\partial \underline{u}_j\underline{p}}{\partial x_j} \\ &- \frac{\gamma-1}{2}\frac{\partial \underline{\rho}\underline{u}_j\underline{u}_k\underline{u}_k}{\partial x_j} + (\gamma-1)\frac{\partial}{\partial x_j}\left[\frac{c_p\mu}{Pr}\frac{\partial \underline{T}}{\partial x_j}\right] \\ &+ (\gamma-1)\frac{\partial}{\partial x_j}\left[\mu\underline{u}_i\left(\frac{\partial \underline{u}_i}{\partial x_j} + \frac{\partial \underline{u}_j}{\partial x_i}\right)\right] \\ &- \frac{2}{3}(\gamma-1)\delta_{ij}\frac{\partial}{\partial x_j}\left[\mu\underline{u}_i\frac{\partial \underline{u}_k}{\partial x_k}\right],\end{aligned} \tag{7}$$

where Θ_0 represents the source terms from the continuity equation, Θ_i (where $i = 1, 2, 3$) represents the three components of the source terms from momentum equations and Θ_4 represents the source terms from the energy equation. Note that the Einstein's convention is only applied for indices, $i = 1, 2, 3$. The under-bar operator in Eqs. (5)–(7) denotes the sum of the base quantity and fluctuating turbulent quantities, i.e., $\underline{q} = \bar{q} + \hat{q} + \breve{q}$.

The propagators on the left-hand side are linearized and are written as

$$\frac{\partial \rho^\perp}{\partial t} + \frac{\partial}{\partial x_j}\left(\underline{\rho}u_j^\perp + \rho^\perp\underline{u}_j\right) = \Theta_0, \tag{8}$$

$$\begin{aligned}&\frac{\partial}{\partial t}\left(\underline{\rho}u_i^\perp + \rho^\perp\underline{u}_i\right) + \frac{\partial}{\partial x_j}\left(\underline{\rho}\underline{u}_iu_j^\perp + \underline{\rho}u_i^\perp\underline{u}_j + \rho^\perp\underline{u}_i\underline{u}_j\right) \\ &+ \frac{\partial p^\perp}{\partial x_j}\delta_{ij} - \frac{\partial}{\partial x_j}\left[\mu\left(\frac{\partial u_i^\perp}{\partial x_j} + \frac{\partial u_j^\perp}{\partial x_i}\right)\right] \\ &+ \frac{2}{3}\frac{\partial}{\partial x_j}\left[\mu\frac{\partial u_k^\perp}{\partial x_k}\right] = \Theta_i,\end{aligned} \tag{9}$$

and

$$\begin{aligned}&\frac{\partial p^\perp}{\partial t} + \frac{\gamma-1}{2}\frac{\partial}{\partial t}\left(\rho^\perp\underline{u}_k\underline{u}_k + 2\underline{\rho}u_k^\perp\underline{u}_k\right) \\ &+ \frac{\gamma-1}{2}\frac{\partial}{\partial x_j}\left(\rho^\perp\underline{u}_j\underline{u}_k\underline{u}_k + \underline{\rho}u_j^\perp\underline{u}_k\underline{u}_k + 2\underline{\rho}\underline{u}_ju_k^\perp\underline{u}_k\right) \\ &+ \gamma\frac{\partial}{\partial x_j}\left(u_j^\perp\underline{p} + \underline{u}_jp^\perp\right) - (\gamma-1)\frac{\partial}{\partial x_j}\left[\frac{c_p\mu}{Pr}\frac{\partial T^\perp}{\partial x_j}\right] \\ &- (\gamma-1)\frac{\partial}{\partial x_j}\left[\mu u_i^\perp\left(\frac{\partial \underline{u}_i}{\partial x_j} + \frac{\partial \underline{u}_j}{\partial x_i}\right) + \mu\underline{u}_i\left(\frac{\partial u_i^\perp}{\partial x_j} + \frac{\partial u_j^\perp}{\partial x_i}\right)\right] \\ &+ (\gamma-1)\frac{2}{3}\delta_{ij}\frac{\partial}{\partial x_j}\left[\mu u_i^\perp\frac{\partial \underline{u}_k}{\partial x_k} + \mu\underline{u}_i\frac{\partial u_k^\perp}{\partial x_k}\right] = \Theta_4,\end{aligned} \tag{10}$$

where the superscript $\perp$ on the field-variables denotes the summation of the radiating fluctuations due to anisotropic and isotropic turbulence respectively, i.e., $q^\perp = q' + q''$.

Miller[27] found the solution to Eqs. (8)–(10) using vector Green's function, which satisfies

$$\frac{\partial \rho_g^{\perp n}}{\partial t} + \frac{\partial}{\partial x_j}\left(\underline{\rho}u_{j,g}^{\perp n} + \rho_g^{\perp n}\underline{u}_j\right) = \delta(\mathbf{x}-\mathbf{y})\delta(t-\tau)\delta_{0n}, \tag{11}$$

$$\begin{aligned}&\frac{\partial}{\partial t}\left(\underline{\rho}u_{i,g}^{\perp n} + \rho_g^{\perp n}\underline{u}_i\right) + \frac{\partial}{\partial x_j}\left(\underline{\rho}\underline{u}_iu_{j,g}^{\perp n} + \underline{\rho}u_{i,g}^{\perp n}\underline{u}_j + \rho_g^{\perp n}\underline{u}_i\underline{u}_j\right) \\ &+ \frac{\partial p_g^{\perp n}}{\partial x_j}\delta_{ij} - \frac{\partial}{\partial x_j}\left[\mu\left(\frac{\partial u_{i,g}^{\perp n}}{\partial x_j} + \frac{\partial u_{j,g}^{\perp n}}{\partial x_i}\right)\right] \\ &+ \frac{2}{3}\frac{\partial}{\partial x_j}\left[\mu\frac{\partial u_{k,g}^{\perp n}}{\partial x_k}\right] = \delta(\mathbf{x}-\mathbf{y})\delta(t-\tau)\delta_{in},\end{aligned} \tag{12}$$

and

$$\begin{aligned}&\frac{\partial p_g^{\perp n}}{\partial t} + \frac{\gamma-1}{2}\frac{\partial}{\partial t}\left(\rho_g^{\perp n}\underline{u}_k\underline{u}_k + 2\underline{\rho}u_{k,g}^{\perp n}\underline{u}_k\right) \\ &+ \frac{\gamma-1}{2}\frac{\partial}{\partial x_j}\left(\rho_g^{\perp n}\underline{u}_j\underline{u}_k\underline{u}_k + \underline{\rho}u_{j,g}^{\perp n}\underline{u}_k\underline{u}_k + 2\underline{\rho}\underline{u}_ju_{k,g}^{\perp n}\underline{u}_k\right) \\ &+ \gamma\frac{\partial}{\partial x_j}\left(u_{j,g}^{\perp n}\underline{p} + \underline{u}_jp_g^{\perp n}\right) - (\gamma-1)\frac{\partial}{\partial x_j}\left[\frac{c_p\mu}{Pr}\frac{\partial T_g^{\perp n}}{\partial x_j}\right] \\ &- (\gamma-1)\frac{\partial}{\partial x_j}\left[\mu u_{i,g}^{\perp n}\left(\frac{\partial \underline{u}_i}{\partial x_j} + \frac{\partial \underline{u}_j}{\partial x_i}\right)\right. \\ &\left.+\mu\underline{u}_i\left(\frac{\partial u_{i,g}^{\perp n}}{\partial x_j} + \frac{\partial u_{j,g}^{\perp n}}{\partial x_i}\right)\right] + (\gamma-1)\frac{2}{3}\delta_{ij} \\ &\times\frac{\partial}{\partial x_j}\left[\mu u_{i,g}^{\perp n}\frac{\partial \underline{u}_k}{\partial x_k} + \mu\underline{u}_i\frac{\partial u_{k,g}^{\perp n}}{\partial x_k}\right] = \delta(\mathbf{x}-\mathbf{y})\delta(t-\tau)\delta_{4n}.\end{aligned} \tag{13}$$

The vector Green's function is written in terms of field-variable, $q_{k,g}^{\perp n} = [\rho_g^{\perp n}, \boldsymbol{u}_{i,g}^{\perp n}, p_g^{\perp n}]^T$, which satisfies Eqs. (11)–(13). The subscript g denotes the Green's function, $\mathbf{x}$ and $\mathbf{y}$ represents the observer location and source location, respectively, δ is the Dirac delta function, and τ is the source emission time.

Using a convolution integral, the solution to the above Eqs. (11)–(13) can be written as

$$q_k^\perp(\mathbf{x}, t) = \int_{-\infty}^{\infty}\ldots\int_{-\infty}^{\infty}\sum_{j=0}^{4} q_{g,k}^{\perp j}(\mathbf{x}, t; \mathbf{y}, \tau)\Theta_j(\mathbf{y}, \tau)d\tau d\mathbf{y}. \tag{14}$$

Using the Wiener-Khinchin theorem,[28] we can define the spectral density as the inverse Fourier transform of the auto-correlation function as

$$S_k^\perp(\mathbf{x}, \omega) = \int_{-\infty}^{\infty}\langle q_k^\perp(\mathbf{x}, t)q_k^\perp(\mathbf{x}, t+\tau^\dagger)\rangle\exp\left[i\omega\tau^\dagger\right]d\tau^\dagger. \tag{15}$$

Making simplifications after substituting Eq. (14) in Eq. (15) and using the definition of auto-correlation, we write the spectral density of pressure as

$$S_4^{\perp}(\mathbf{x},\omega) = \int_{-\infty}^{\infty}\cdots\int_{-\infty}^{\infty}\sum_{m=0}^{4}\sum_{n=0}^{4}\tilde{p}_g^{*\perp,m}(\mathbf{x};\mathbf{y},\omega) \times \tilde{p}_g^{\perp,n}(\mathbf{x};\mathbf{y}+\boldsymbol{\eta},\omega)R_{m,n}^{\perp}(\mathbf{y},\boldsymbol{\eta},\tau) \times \exp[i\omega\tau]d\tau d\boldsymbol{\eta}d\mathbf{y}. \quad (16)$$

Here, the two-point space-time cross-correlation of the source terms is denoted by $R_{m,n}(\mathbf{y},\boldsymbol{\eta},\tau)$ and written as

$$R_{m,n}^{\perp}(\mathbf{y},\boldsymbol{\eta},\tau) = \langle\Theta_m(\mathbf{y},\tau)\Theta_n(\mathbf{y}+\boldsymbol{\eta},\tau+\Delta\tau)\rangle = \int_{-\infty}^{\infty}\Theta_m(\mathbf{y},\tau)\Theta_n(\mathbf{y}+\boldsymbol{\eta},\tau+\Delta\tau)d\Delta\tau, \quad (17)$$

where $\boldsymbol{\eta} = (\xi,\eta,\zeta)$ is a source separation vector pointing from one source location to the other, while $\Delta\tau$ is the time delay between the two sources. The tilde operator $\tilde{q}$ represents the Fourier transform on the field variable q, while the asterisk superscript q^* represents the complex conjugate of the complex variable q.

To evaluate Eq. (16), we require the vector Green's function as well as the two-point cross-correlation source term(s). In Sec. II B, we derive the vector Green's function for pressure, and we identify the source terms for BBSAN in Sec. II C.

B. Vector Green's function

The refraction effects for a single stream unheated jet in the sideline direction are minimal.[29–31] We also assume that the environment is quiescent for deriving the vector Green's function. Atmospheric attenuation due to viscosity, humidity, and heat conduction can be calculated from the work of Bass *et al.*[32] at different frequencies. Standards such as ISO 9613-1:1993 and ANSI S1.26-1995 use minor variations of the same formula. The attenuation at 20 °C at atmospheric pressure with 0% relative humidity for a sound wave with a frequency of 10 kHz is 0.05 dB/m. Considerable losses have to be taken into account for high frequencies and over large distances. However, for the current application (frequency, $f < 0.1$ MHz; distance, $d < 20$ m), we can neglect the viscous effects on the linear sound propagation.

To obtain the vector Green's function for pressure, we perform partial time derivative on the energy Green's Eq. (13) and take a gradient of the momentum Green's Eq. (12). We use the relation $\gamma p_\infty = c_\infty^2\rho_\infty$, multiply c_∞^2 to the gradient of the momentum Green's equation, and subtract the result from the time derivative of the energy Green's equation. We obtain

$$\frac{\partial^2 p_g^{\perp n}}{\partial t^2} - c_\infty^2\frac{\partial^2 p_g^{\perp n}}{\partial x_i^2} = \frac{\partial}{\partial t}[\delta(\mathbf{x}-\mathbf{y})\delta(t-\tau)\delta_{4n}] - c_\infty^2\frac{\partial}{\partial x_i}[\delta(\mathbf{x}-\mathbf{y})\delta(t-\tau)\delta_{in}]. \quad (18)$$

Performing the Fourier transform with respect to time on Eq. (18) we obtain

$$\omega^2\tilde{p}_g^{\perp n} + c_\infty^2\frac{\partial^2\tilde{p}_g^{\perp n}}{\partial x_i^2} = i\omega\delta(\mathbf{x}-\mathbf{y})\delta_{4n} + c_\infty^2\frac{\partial}{\partial x_i}\delta(\mathbf{x}-\mathbf{y})\delta_{in}. \quad (19)$$

The solution to the vector Green's function for pressure is

$$\tilde{p}_g^{\perp n} = \left(-\frac{i\omega}{4\pi c_\infty r} + \frac{1}{4\pi r^2}\right)\frac{(x_i-y_i)}{r}\exp\left[\frac{i\omega r}{c_\infty}\right]\delta_{in} - \frac{i\omega}{4\pi c_\infty^2 r}\exp\left[\frac{i\omega r}{c_\infty}\right]\delta_{4n}, \quad (20)$$

where $r = |\mathbf{x}-\mathbf{y}|$. For the far-field, we can simplify the vector Green's function to

$$\tilde{p}_g^{\perp n}(\mathbf{x},\mathbf{y},\omega) = \frac{-i\omega}{4\pi c_\infty r}\exp\left[\frac{i\omega r}{c_\infty}\right]\left(\frac{x_i}{r}\delta_{in} + \frac{1}{c_\infty}\delta_{4n}\right). \quad (21)$$

Following Tam and Auriault,[33] we obtain

$$\tilde{p}_g^{\perp n}(\mathbf{x},\mathbf{y}+\boldsymbol{\eta},\omega) = \tilde{p}_g^{\perp n}(\mathbf{x},\mathbf{y},\omega)\exp\left[-\frac{i\omega\mathbf{x}\cdot\boldsymbol{\eta}}{c_\infty r}\right], \quad (22)$$

which is a relation for the phase difference between two stream-wise source locations within a jet after the far-field assumption has been made. Next, we identify the source terms for shock-associated noise.

C. Source terms for shock-associated noise

The source term in Eq. (16) is the two-point cross-correlation of the sources of Eqs. (5)–(7). The two-point cross-correlation can be written as a matrix containing 25 elements formed from the cross-correlation of Eqs. (5)–(7) as

$$R_{m,n}^{\perp} = \begin{bmatrix} R_{00}^{\perp} & R_{01}^{\perp} & R_{02}^{\perp} & R_{03}^{\perp} & R_{04}^{\perp} \\ R_{10}^{\perp} & R_{11}^{\perp} & R_{12}^{\perp} & R_{13}^{\perp} & R_{14}^{\perp} \\ R_{20}^{\perp} & R_{21}^{\perp} & R_{22}^{\perp} & R_{23}^{\perp} & R_{24}^{\perp} \\ R_{30}^{\perp} & R_{31}^{\perp} & R_{32}^{\perp} & R_{33}^{\perp} & R_{34}^{\perp} \\ R_{40}^{\perp} & R_{41}^{\perp} & R_{42}^{\perp} & R_{43}^{\perp} & R_{44}^{\perp} \end{bmatrix}. \quad (23)$$

Here, $R_{00}^{\perp}$ represents the two-point cross-correlation of continuity equation with itself, $R_{01}^{\perp}$ to $R_{03}^{\perp}$ represents the two-point cross-correlation of the continuity equation with the three components of the momentum equations, while $R_{04}^{\perp}$ represents the two-point cross-correlation of the continuity equation with the energy equation. Similarly, other terms represent the two-point cross-correlation of the momentum equations with the continuity and energy equation, and energy equation with the continuity and momentum equations.

As an example, the two-point cross-correlation for the continuity-continuity equation can be written as

$$R_{0,0}^{\perp} = \langle\Theta_0(\mathbf{y},\tau),\Theta_0(\mathbf{y}+\boldsymbol{\eta},\tau+\Delta\tau)\rangle = \left\langle\left(-\frac{\partial\underline{\rho}^{(1)}}{\partial\tau} - \frac{\partial\underline{\rho}^{(1)}\underline{u}_j^{(1)}}{\partial y_j}\right),\left(-\frac{\partial\underline{\rho}^{(2)}}{\partial\tau} - \frac{\partial\underline{\rho}^{(2)}\underline{u}_m^{(1)}}{\partial y_m}\right)\right\rangle. \quad (24)$$

Expanding Eq. (24), we can write the two-point cross-correlation as

$$R^{\perp}_{0,0}(\mathbf{y},\boldsymbol{\eta},\tau) = \left\langle \frac{\partial \underline{\rho}^{(1)}}{\partial \tau}, \frac{\partial \underline{\rho}^{(2)}}{\partial \tau} \right\rangle + \left\langle \frac{\partial \underline{\rho}^{(1)}}{\partial \tau}, \frac{\partial \underline{\rho}^{(2)} \underline{u}^{(2)}_m}{\partial y_m} \right\rangle + \left\langle \frac{\partial \underline{\rho}^{(1)} \underline{u}^{(1)}_j}{\partial y_j}, \frac{\partial \underline{\rho}^{(2)}}{\partial \tau} \right\rangle + \left\langle \frac{\partial \underline{\rho}^{(1)} \underline{u}^{(1)}_j}{\partial y_j}, \frac{\partial \underline{\rho}^{(2)} \underline{u}^{(2)}_m}{\partial y_m} \right\rangle. \tag{25}$$

Expanding all the two-point cross-correlation terms in Eq. (23) will result in 576 terms. In Eqs. (24) and (25), the superscripts (1) and (2) denote the location of two different source terms, one at location $\mathbf{y}$ and the other at $\mathbf{y}+\boldsymbol{\eta}$. The derivatives in the source terms are performed with respect to $\mathbf{y}$ and τ because they represent the source position and time, respectively.

Following Ribner,[34] we model these two-point cross-correlation terms as

$$R^{\perp}_{m,n} = \mathcal{A} R, \tag{26}$$

where $\mathcal{A}$ represents the magnitude of the two-point cross-correlation source term and R represents the normalized two-point cross-correlation term. The magnitude is directly obtained from the source term, while the normalized two-point cross-correlation term can be obtained from numerical computations like LES or direct numerical simulations (DNS), or can be estimated from theoretical or experimental results. Note that the normalized two-point cross-correlation term will be different depending on whether the source terms are isotropic ($\breve{R}$), anisotropic ($\hat{R}$), or is an interaction of the anisotropic turbulence with the isotropic turbulence ($\hat{\breve{R}}$). For example, we expand the first term of the continuity-continuity correlation into its respective base flow, isotropic fluctuation, and anisotropic fluctuation components as

$$\begin{aligned}\left\langle \frac{\partial \underline{\rho}^{(1)}}{\partial \tau}, \frac{\partial \underline{\rho}^{(2)}}{\partial \tau} \right\rangle = {} & \frac{\partial \bar{\rho}^{(1)}}{\partial \tau}\frac{\partial \bar{\rho}^{(2)}}{\partial \tau} + \frac{\partial \bar{\rho}^{(1)}}{\partial \tau}\frac{\breve{\rho}^{(2)}}{\breve{\tau}^{(2)}_s} + \frac{\partial \bar{\rho}^{(1)}}{\partial \tau}\frac{\hat{\rho}^{(2)}}{\hat{\tau}^{(2)}_s} + \frac{\breve{\rho}^{(1)}}{\breve{\tau}^{(1)}_s}\frac{\partial \bar{\rho}^{(2)}}{\partial \tau} \\ & + \frac{\breve{\rho}^{(1)}}{\breve{\tau}^{(1)}_s}\frac{\breve{\rho}^{(2)}}{\breve{\tau}^{(2)}_s}\breve{R} + \frac{\breve{\rho}^{(1)}}{\breve{\tau}^{(1)}_s}\frac{\hat{\rho}^{(2)}}{\hat{\tau}^{(2)}_s}\hat{\breve{R}} \\ & + \frac{\hat{\rho}^{(1)}}{\hat{\tau}^{(1)}_s}\frac{\partial \bar{\rho}^{(2)}}{\partial \tau} + \frac{\hat{\rho}^{(1)}}{\hat{\tau}^{(1)}_s}\frac{\breve{\rho}^{(2)}}{\breve{\tau}^{(2)}_s}\hat{\breve{R}} + \frac{\hat{\rho}^{(1)}}{\hat{\tau}^{(1)}_s}\frac{\hat{\rho}^{(2)}}{\hat{\tau}^{(2)}_s}\hat{R}.\end{aligned} \tag{27}$$

Since each respective term of the two-point cross-correlation is decomposed into three components, the decomposed first term of Eq. (25) is shown in Eq. (27), which consists of nine different terms. The magnitude of the space or time derivatives of the fluctuating terms is approximated using an order of magnitude analysis. Their magnitude is modeled as the ratio of the fluctuating term with an appropriate time or length scale corresponding to that term. From Eq. (26), an appropriate normalized two-point cross-correlation term is multiplied with the magnitude of the source term. The second, third, and fourth term in Eq. (25) consists of 27, 27, and 81 terms, respectively, if expanded. Note that the correlation between two constant quantities, or a fluctuating quantity and a constant is zero, thus we can eliminate five of the nine terms in Eq. (27). Decomposing each of the 576 terms and evaluating each term individually is tedious. Also, one of the terms within the energy-energy correlation can be decomposed to 6561 further terms. To find the BBSAN source term within all possible source term expansions, we eliminate various source terms that do not correlate with the scaling of BBSAN. We then focus our modeling effort on the physical mechanism of BBSAN and try to identify terms that are related.

Lighthill[35] noted that *"The viscous stresses are just as unimportant inside the flow as they are known to be outside it."* For air, we can neglect the viscous source terms as their magnitude are five orders lower than the other source terms. Now, the number of terms that require evaluation is drastically reduced. The remaining source terms from the momentum and energy equations are written as

$$\Theta_i = -\frac{\partial \underline{\rho}\underline{u}_i}{\partial t} - \frac{\partial \underline{\rho}\underline{u}_i\underline{u}_j}{\partial x_j} - \frac{\partial \underline{p}}{\partial x_j}\delta_{ij}, \tag{28}$$

and

$$\Theta_4 = -\frac{\partial \underline{p}}{\partial t} - \frac{\gamma-1}{2}\frac{\partial \underline{\rho}\underline{u}_k\underline{u}_k}{\partial t} - \gamma\frac{\partial \underline{u}_j\underline{p}}{\partial x_j} - \frac{\gamma-1}{2}\frac{\partial \underline{\rho}\underline{u}_j\underline{u}_k\underline{u}_k}{\partial x_j}. \tag{29}$$

Based on the physics of BBSAN, we know that the source term depends on the interaction of shocks with the large-scale turbulent structures. From the remaining source terms shown in Eqs. (28) and (29), we find the terms that represent the shock strength as well as the large-scale turbulent structures. The shock strength is either represented by the gradient of mean pressure or the gradient of the mean density, while the large turbulent structures are represented by anisotropic velocity. In the current paper, we use the RANS solutions to obtain the mean quantities, while the isotropic and anisotropic fluctuations are modeled based on theoretical and experimental results. However, given an instantaneous flow-field, the aerodynamic fluctuating quantities can be separated into isotropic and anisotropic fluctuations by using decomposition methods such as proper orthogonal decomposition or singular value decomposition.

We can see that the third term in Eq. (28) and the first term in Eq. (29), i.e., gradient of pressure and the time derivative of pressure do not represent the source term for BBSAN. Since the shocks are represented by the mean pressures, the fluctuating pressures do not indicate the shock locations as well as the shock strength. The time derivatives of mean quantities are zero, while the spatial derivative of the mean quantities is a constant. Hence, the two-point cross-correlation of both these terms with any of the other remaining terms is zero. Similarly, the first term in Eq. (28) and the second term in Eq. (29) can be eliminated as both involve time derivative terms. However, the two-point cross-correlation of the second term in Eq. (29) is used by

Tam and Auriault[33] as a source of fine-scale mixing noise. They proposed this source term using the gas kinetic theory. The same source term is independently obtained by the approach in the present paper. The remaining terms are

$$R^{(1)} = \left\langle \frac{\partial \underline{\rho}^{(1)} \underline{u}_i^{(1)} \underline{u}_j^{(1)}}{\partial y_j}, \frac{\partial \underline{\rho}^{(2)} \underline{u}_l^{(2)} \underline{u}_m^{(2)}}{\partial y_m} \right\rangle, \tag{30a}$$

$$R^{(2)} = \gamma \left\langle \frac{\partial \underline{\rho}^{(1)} \underline{u}_i^{(1)} \underline{u}_j^{(1)}}{\partial y_j}, \frac{\partial \underline{u}_m^{(2)} \underline{p}^{(2)}}{\partial y_m} \right\rangle, \tag{30b}$$

$$R^{(3)} = \frac{\gamma - 1}{2} \left\langle \frac{\partial \underline{\rho}^{(1)} \underline{u}_i^{(1)} \underline{u}_j^{(1)}}{\partial y_j}, \frac{\partial \underline{\rho}^{(2)} \underline{u}_m^{(2)} \underline{u}_n^{(2)} \underline{u}_n^{(2)}}{\partial y_m} \right\rangle, \tag{30c}$$

$$R^{(4)} = \gamma^2 \left\langle \frac{\partial \underline{u}_j^{(1)} \underline{p}^{(1)}}{\partial y_j}, \frac{\partial \underline{u}_m^{(2)} \underline{p}^{(2)}}{\partial y_m} \right\rangle, \tag{30d}$$

$$R^{(5)} = \frac{\gamma(\gamma - 1)}{2} \left\langle \frac{\partial \underline{u}_j^{(1)} \underline{p}^{(1)}}{\partial y_j}, \frac{\partial \underline{\rho}^{(2)} \underline{u}_m^{(2)} \underline{u}_n^{(2)} \underline{u}_n^{(2)}}{\partial y_m} \right\rangle, \tag{30e}$$

and

$$R^{(6)} = \frac{(\gamma - 1)^2}{4} \left\langle \frac{\partial \underline{\rho}^{(1)} \underline{u}_j^{(1)} \underline{u}_k^{(1)} \underline{u}_k^{(1)}}{\partial y_j}, \frac{\partial \underline{\rho}^{(2)} \underline{u}_m^{(2)} \underline{u}_n^{(2)} \underline{u}_n^{(2)}}{\partial y_m} \right\rangle, \tag{30f}$$

which are candidates for source terms of BBSAN. We simplify Eq. (30) as per Eq. (26) and obtain

$$R^{(1)} = \frac{\partial \bar{\rho}^{(1)} \bar{u}_i^{(1)}}{\partial y_j} \frac{\partial \bar{\rho}^{(2)} \bar{u}_l^{(2)}}{\partial y_m} \hat{u}_j^{(1)} \hat{u}_m^{(2)} \hat{R}, \tag{31a}$$

$$R^{(2)} = \gamma \frac{\partial \bar{\rho}^{(1)} \bar{u}_i^{(1)}}{\partial y_j} \frac{\partial \bar{p}^{(2)}}{\partial y_m} \hat{u}_j^{(1)} \hat{u}_m^{(2)} \hat{R}, \tag{31b}$$

$$R^{(3)} = \frac{\gamma - 1}{2} \frac{\partial \bar{\rho}^{(1)} \bar{u}_i^{(1)}}{\partial y_j} \frac{\partial \bar{\rho}^{(2)} \bar{u}_n^{(2)} \bar{u}_n^{(2)}}{\partial y_m} \hat{u}_j^{(1)} \hat{u}_m^{(2)} \hat{R}, \tag{31c}$$

$$R^{(4)} = \gamma^2 \frac{\partial \bar{p}^{(1)}}{\partial y_j} \frac{\partial \bar{p}^{(2)}}{\partial y_m} \hat{u}_j^{(1)} \hat{u}_m^{(2)} \hat{R}, \tag{31d}$$

$$R^{(5)} = \frac{\gamma(\gamma - 1)}{2} \frac{\partial \bar{p}^{(1)}}{\partial y_j} \frac{\partial \bar{\rho}^{(2)} \bar{u}_n^{(2)} \bar{u}_n^{(2)}}{\partial y_m} \hat{u}_j^{(1)} \hat{u}_m^{(2)} \hat{R}, \tag{31e}$$

and

$$R^{(6)} = \frac{(\gamma - 1)^2}{4} \frac{\partial \bar{\rho}^{(1)} \bar{u}_k^{(1)} \bar{u}_k^{(1)}}{\partial y_j} \frac{\partial \bar{\rho}^{(2)} \bar{u}_n^{(2)} \bar{u}_n^{(2)}}{\partial y_m} \hat{u}_j^{(1)} \hat{u}_m^{(2)} \hat{R}. \tag{31f}$$

In Sec. II D, we identify the BBSAN source term by comparing the scaling of the source term with experimental scaling laws of BBSAN. After identifying the source term, and substituting the source term and vector Green's function in Eq. (16), we integrate Eq. (16) with respect to τ and $\boldsymbol{\eta}$ in Sec. II E to obtain a closed-form model for BBSAN.

D. Scaling of source terms with off-design parameter

We perform a scaling analysis of Eq. (30) with the off-design parameter β to identify the source of BBSAN. We use steady RANS computational fluid dynamics (CFD) to find the meanflow properties of the jet. The RANS simulation is closed by the Menter[36] $K - \Omega$ shear stress transport model, where K represents the turbulent kinetic energy and Ω represents the specific dissipation rate. The FUN3D[37] code is used to simulate the RANS solutions. The nozzle used for the simulation is the SMC016 nozzle, where SMC stands for small metal chevron. SMC016 is an axisymmetric convergent-divergent nozzle with design Mach number, $M_d = 1.5$. The domain is extended to $100\,D$ in the downstream direction, and $50\,D$ in the cross-stream direction, where $D = 0.0508$ m is the diameter of the nozzle exit. As the nozzle is axisymmetric, the mesh is extruded by rotating it 90°. Abdol-Hamid *et al.*[38] performed nozzle simulations on the ARN1 nozzle using FUN3D. We use the same boundary conditions as Abdol-Hamid *et al.*[38] Symmetric plane boundary conditions are applied on the sides to save computational expense. Total pressure and total temperature are specified at the inlet of the nozzle, atmospheric pressure is specified at the outlet, an adiabatic no-slip wall is specified at the nozzle walls, and a zero free-stream velocity is specified on the top and side boundaries of the domain.

The NPR corresponding to the ideal operating condition for the SMC016 nozzle is 3.67. The CFD simulations are performed at NPR = [3.693, 3.745, 3.858, 4.043, 4.32, 4.7, 5.2, 6] for under-expanded cases, and at NPR = [2.4, 2.75, 3.1, 3.382, 3.503, 3.593, 3.643] for over-expanded cases. All the cases correspond to an unheated jet with TTR = 1.0. The magnitude of all the source terms from Eq. (31) are evaluated for scaling analysis using RANS results. The magnitude of $\hat{u}_j \hat{u}_m$ in the source terms from Eq. (31) is modeled by turbulent kinetic energy, which is obtained directly from the RANS simulations. Note that this approximation is only for the scaling analysis and the anisotropic velocities are modeled using an anisotropic spectrum in Sec. II E, for predicting the BBSAN. The normalized two-point cross-correlation is not considered for scaling analysis.

The scaling of BBSAN for both under-expanded as well as over-expanded cases is shown in Fig. 4. The normalized intensity of the source term, obtained using RANS CFD solutions, is plotted against the off-design parameter β in Fig. 4. For the over-expanded case, none of the terms except term-4 scales with β^4. Term-4 is initially constant, because the operating condition of the jet is very close to the ideally expanded condition. Only very weak shocks are present in the jet exhaust and other noise sources dominate BBSAN at this condition. The BBSAN scales as β^4 for NPR = [3.503, 3.382, 3.1]. Mach disk formation starts when we decrease the NPR less than 3.1. Therefore, an abrupt drop of amplitude for term-4 occurs at NPR = 2.4. For the under-expanded condition, term-4 is the most correlated with β^4 among all possible source terms. Term-2 and term-5 show rough scaling with β^2 because of the presence of the gradient of pressure term. Term-1, 3, and 6 are independent of β and are not candidates for shock-noise. Term-4 scales very well as β^4 except at NPR = 3.693, which is very close to the ideally expanded condition of NPR = 3.67. From the scaling analysis of Eq. (31), it

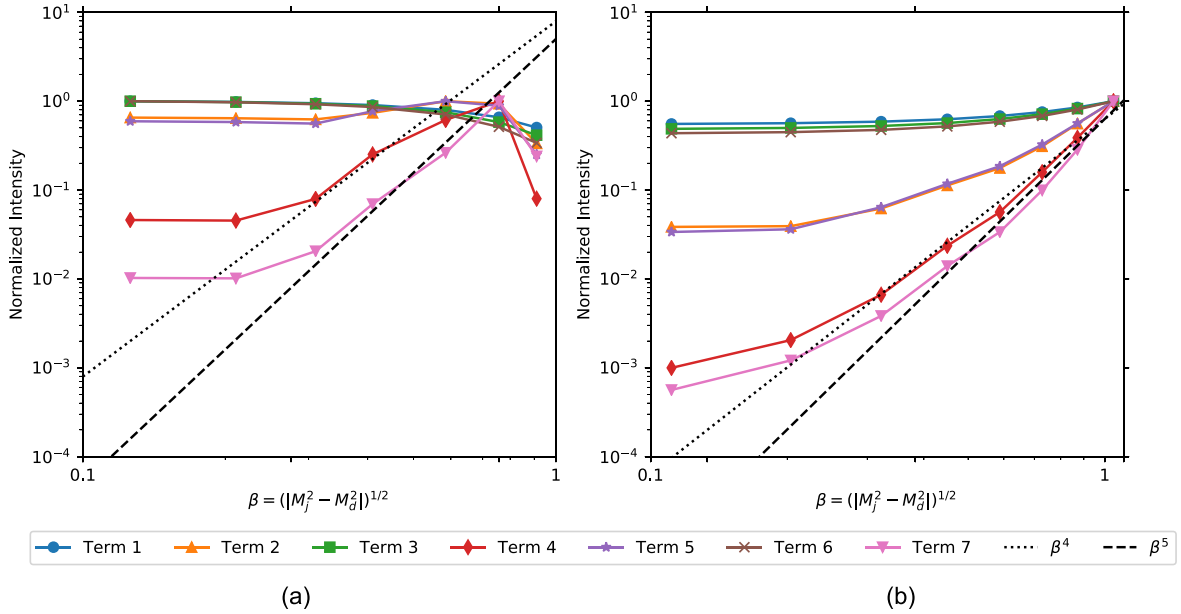

FIG. 4. (Color online) Scaling of BBSAN source term for (a) over-expanded case and (b) under-expanded case.

could be inferred that any bi-product of the gradient of mean pressure term can scale as β^4. However, that is not the case, and to further confirm that there are no additional term that scales as β^4, we perform the scaling analysis of the term

$$R^{(7)} = \frac{\partial \bar{p}^{(1)}}{\partial y_j}\frac{\partial \bar{p}^{(2)}}{\partial y_m}, \tag{32}$$

as an example. Note that although this term is present in the momentum equation, the two-point cross-correlation of this term is zero because of the presence of only mean quantities. The scaling of the term-7 from Eq. (32) is shown in Fig. 4. Figure 4 shows that the term-7 roughly scales as β^5. Hence, the only term that scales as β^4 is term-4.

The source term for BBSAN is given by Eq. (31d), based on the correlation with the variation of NPR. This term is the product of the gradient of mean pressure with the anisotropic velocity. The gradient of mean pressure represents the shock strength while the anisotropic velocities represent the large-scale structures in the shear layer. This term is obtained from the acoustic analogy based on the decomposition of the Navier-Stokes equations. The source term is evaluated by making various empirical assumptions such as modeling the two-point cross-correlation as well as the anisotropic velocities while using a RANS simulation. In Sec. II E, we evaluate the spectral density of pressure by modeling the anisotropic normalized two-point cross-correlation term and substituting the arguments in Eq. (16).

E. Evaluation of the spectral density

Following Ribner,[34] we model the normalized two-point cross-correlation as

$$\hat{R} = \exp\left[-\frac{|\tau|}{\tau_s}\right]\exp\left[-\frac{(\xi - u_c\tau)^2}{l^2}\right]\exp\left[-\frac{(\eta^2+\zeta^2)}{l_\perp^2}\right], \tag{33}$$

where τ_s is the time scale, l and $l_\perp$ are the length scales in the streamwise and cross-stream direction, respectively, and u_c is the eddy convection speed.

We substitute the source terms of Eqs. (31d) and (33), and the solution to the vector Green's function of Eqs. (21) and (22) in Eq. (16), and integrate the equation with respect to τ and $\boldsymbol{\eta}$. We follow Morris and Miller[13] to evaluate the gradient of pressure at two different locations by taking the Fourier transform of one term. The resulting spectral density is very similar to the model of Morris and Miller[13] because we use the same normalized two-point cross-correlation model. However, the source terms in the two models are different. After integrating, we obtain

$$S_4^{\perp}(\mathbf{x},\omega) = \frac{\gamma^2\omega^2}{16\pi\sqrt{\pi}c_\infty^4 r^2}\int\int_{-\infty}^{\infty} l_\perp^2 l\tau_s \exp\left[-\frac{\omega^2 l_\perp^2 \sin^2\theta}{4c_\infty^2}\right]\frac{\partial \bar{p}}{\partial y_j}(\mathbf{y})\hat{u}_j(\mathbf{y})$$
$$\times\left[\int_{-\infty}^{\infty}\frac{\exp\left[-l^2\left(\kappa - \frac{\omega\cos\theta}{c_\infty}\right)^2\Big/4\right]}{\left[1+\left(1-M_c\cos\theta+\frac{u_c\kappa}{\omega}\right)^2\omega^2\tau_s^2\right]}\frac{\partial \bar{p}}{\partial y_m}(\kappa,y_2,y_3)d\kappa\right]\cdot\hat{u}_m(\mathbf{y})d\mathbf{y}, \tag{34}$$

where κ is the wavenumber, $M_c = u_c c_\infty^{-1}$ represents the convective Mach number, and θ is the polar observer angle. The implementation of Eq. (34) is performed similarly to Morris and Miller.[13] The mean values are obtained using the RANS $K-\Omega$ SST model. The gradient of mean pressure and the turbulent kinetic energy from the RANS simulations are shown in Fig. 5, corresponding to NPR = 5.2 and TTR = 1.0. The convection velocity of large-scale turbulent structures is modeled as $u_c = \bar{u}$. The dissipation rate ε is obtained using $\epsilon = 0.09K\Omega$.[36] A length scale and time scale are estimated from turbulent kinetic energy and dissipation rate as $l = c_l K^{3/2}\epsilon^{-1}$, $l_\perp = 0.33l$, and $\tau_s = c_\tau K\epsilon^{-1}$, where c_τ and c_l are constants.

The composite energy spectrum for velocity can be modeled based on Kolmogorov[39] theory as

$$E_u(\kappa) = c_u \epsilon^{2/3}\kappa^{-5/3} f_{L,u}(\kappa L) f_{\eta,u}(\kappa\eta), \tag{35}$$

where the constant $c_u = 1.5$.[40] The spectrum scales as $\kappa^{-5/3}$ in the inertial subrange region and is connected to the energy-containing range and the dissipation range by the composite spectrum proposed by Pope[40] as

$$f_{L,u}(\kappa L) = \left[\frac{\kappa L}{\sqrt{(\kappa L)^2 + 6.78}}\right]^{11/3}, \tag{36a}$$

and

$$f_{\eta,u}(\kappa\eta) = \exp\left[-2.1\left(\left[(\kappa\eta)^4 + 0.0256\right]^{1/4} - 0.4\right)\right]. \tag{36b}$$

The anisotropic velocities are modeled based on the numerical and theoretical work of Ishihara *et al.*[41] They showed that the anisotropic energy spectrum for velocity in the homogeneous turbulent shear layer scales as

$$\hat{E}_u(\kappa) = \hat{c}_u \epsilon^{1/3}\kappa^{-7/3} f_{L,u}(\kappa L) f_{\eta,u}(\kappa\eta). \tag{37}$$

The amplitude in the energy-containing range for anisotropic spectra is matched with the Kolmogorov[39] theory from Eq. (35) using the parameter $\hat{c}_u$. The isotropic spectrum is obtained by subtracting the anisotropic spectrum from the total velocity spectrum. The isotropic and anisotropic energy spectra are a function of space depending on the local turbulent kinetic energy (K) and the local specific dissipation rate (Ω) at each point inside the domain. The energy spectra for a point in the shear layer of the jet exhaust is shown in Fig. 6. The anisotropy of the large-scale structures is captured using an anisotropic energy spectrum. Figure 6 shows that the energy contained at low wavenumbers is higher for the anisotropic spectrum. This corresponds to the large-scale coherent structures that have most of its energy at low wavenumbers. Conversely, the energy contained at high wavenumbers is higher for the isotropic spectrum, which corresponds to the energy from the fine-scale incoherent structures. The anisotropic velocity can be obtained from the energy spectrum as

$$\hat{u}_1(\mathbf{y},\tau) = \left[c_1 \int_{\kappa_1}^{\kappa_2} \hat{E}_u(\mathbf{y},\kappa,\tau)d\kappa\right]^{1/2}, \tag{38a}$$

and

$$\hat{u}_2(\mathbf{y},\tau) = \hat{u}_3(\mathbf{y},\tau) = \left[c_2 \int_{\kappa_1}^{\kappa_2} \hat{E}_u(\mathbf{y},\kappa,\tau)d\kappa\right]^{1/2}, \tag{38b}$$

where $c_1 = 18/11$ and $c_2 = 2/11$ are empirical constants. The limits of the integrations, κ_1 and κ_2, are determined from the frequency which is being evaluated, i.e., $\omega = c_\infty(\kappa_1 + \kappa_2)/2$. The wavenumbers, κ_1 and κ_2, are related as $\kappa_2 - \kappa_1 = \omega/c_\infty$.

Finally, the numerical integration of Eq. (34) is performed on a structured grid. The CFD solution is interpolated on two different structured grids. One grid is used to perform the discrete Fourier transform (DFT) of the gradient of pressure, while the other grid is for numerical integration of the spectral density of pressure. The wavenumber grid, i.e., the grid on which the DFT is performed, extends from $0.00196D$ to $30D$ in the stream-wise direction with 1024 equidistant points and extends from 0 to D in the cross-stream direction with 100 equidistant points. This allows us to resolve $\Delta\kappa = 2.061$ m^{-1} while the wavenumber scale

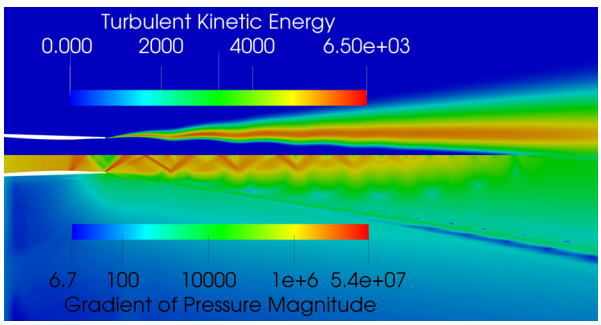

FIG. 5. (Color online) Contours of (Top) turbulent kinetic energy; (Bottom) magnitude of the gradient of mean pressure.

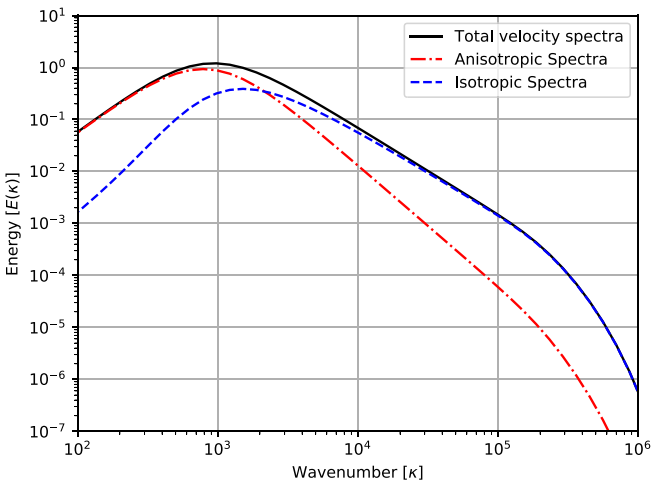

FIG. 6. (Color online) Decomposition of the total energy spectrum of velocity to anisotropic and isotropic spectra.

ranges from -2110.86 to $2110.86\ \mathrm{m}^{-1}$. The DFT is calculated after mirroring the gradient of pressure across $\kappa = 0$ so that the Fourier transform is real and symmetric. The low-frequency component near zero wavenumber is not considered inside the integration because it represents a fictitious amount of energy due to the meanflow of the RANS solution. The volume integration grid extends from $0.00196D$ to $15\,D$ in the stream-wise direction and 0 to D in the cross-stream direction while having 500 and 100 equidistant points, respectively, in each direction. The wavenumber spectrum and the spatial region for obtaining the spectral density are integrated using the trapezoidal rule.

III. RESULTS

A. BBSAN prediction results

The prediction results from Eq. (34) are plotted against the previous prediction model by Morris and Miller[13] and the experimental SHJAR database[5] in Fig. 7. The predictions are compared with the experimental SHJAR database[5] that contains corrections for atmospheric losses. The observer is located at $100\,D$ from the nozzle exit at multiple angles. The predictions and measurements are shown as the SPL per unit Strouhal number versus Strouhal number. The Strouhal number is the non-dimensionalized frequency, which is defined as $St = fD_j/u_j$, where D_j and u_j are the fully-expanded jet diameter and jet velocity, respectively. We first calibrate our model with the experimental results using the $M_j = 1.734$ case for the observer at $\theta = 90^\circ$. The constants are calibrated once with the experimental results for one operating condition, and the same constants are used for predicting the BBSAN over a range of conditions. The calibrated constants used in this paper are $c_l = 0.75$ and $c_\tau = 1.75$. The amplitude for the spectral density of BBSAN is scaled using a constant, $A = 10^{0.778} = 6$ for all jet conditions. Same calibration conditions ($M_j = 1.734$; $\theta = 90^\circ$), but different calibration constants are used for the calibration of the Morris and Miller[13] model. The calibration constants used for the Morris and Miller[13] model are $c_l = 1.0$, $c_\tau = 0.6$, and $A = 6$. The predictions performed at multiple angles ranging from $\theta = 70^\circ$ to $\theta = 130^\circ$ for $M_j = 1.734$ are shown in Fig. 7(a), where θ is measured from the downstream jet axis. The predictions are compared with the experimental results at various over-expanded and under-expanded cases ranging from $M_j = 1.294$ to $M_j = 1.8282$ in the sideline direction shown in Fig. 7(b). The maximum SPL of the individual experimental spectrum is annotated in Fig. 7.

When comparing the results from the current model with the experimental results in Fig. 7(a), the prediction results match the peak Strouhal numbers within $\Delta St = 0.1$, while the amplitudes match within 0.5 dB for the peak BBSAN. The predictions from the Morris and Miller[13] model are very similar to the current model predictions. They are offset by a maximum $\Delta \mathrm{St} = 0.15$ and the amplitude is underpredicted by 1 dB at $\theta = 70^\circ$ when compared to

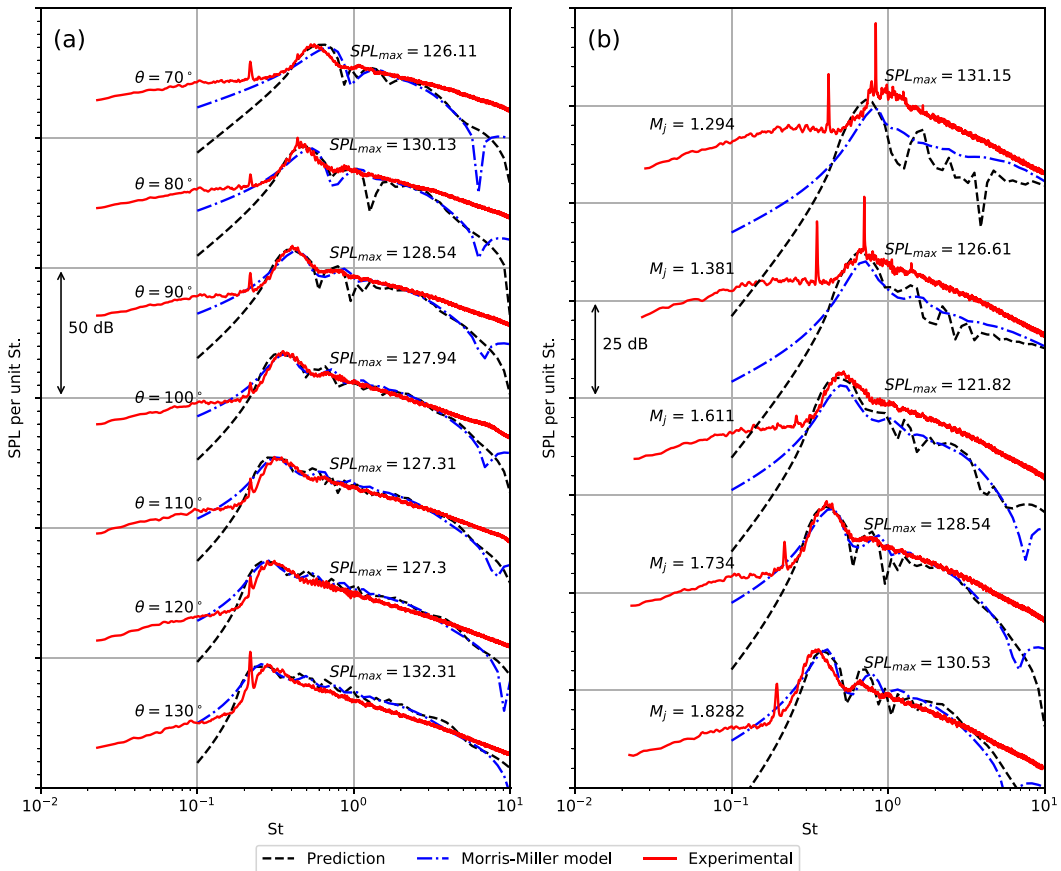

FIG. 7. (Color online) Prediction results for scaling of shock-noise at multiple (a) angles for $M_d = 1.5; M_j = 1.734$ and (b) NPRs in the sideline direction ($\theta = 90^\circ$).

the experimental results. For $\theta = 120°$ and $\theta = 130°$, the current prediction as well as the Morris and Miller[13] prediction over-predicts the multiple harmonics of BBSAN by about 1 and 2 dB, respectively. Using the current prediction model in Fig. 7(b), the peak Strouhal number matches the experimental spectrum within $\Delta St = 0.1$, except for the over-expanded case of $M_j = 1.294$, where the peak Strouhal number is offset by $\Delta St = 0.2$. For $M_j = 1.294$, the current prediction under-predicts the peak SPL by 3 dB. The Morris and Miller[13] model under-predicts the peak SPL by 5 dB, and Strouhal number is offset by $\Delta St = 0.03$ for the $M_j = 1.294$ case. The higher harmonics in the current model predictions are under-predicted by 4 dB for the over-expanded cases, $M_j = 1.294$ and 1.381, while they are under-predicted by 2 dB for the under-expanded case $M_j = 1.611$. The Morris and Miller[13] model under-predicts the higher harmonics by 7 and 6 dB for $M_j = 1.294$ and 1.381, respectively. For the under-expanded case $M_j = 1.611$, the peak SPL is under-predicted by 3 dB, while the higher harmonics are under-predicted by 5 dB by the Morris and Miller[13] model. There is over-prediction in the second harmonic by 3 dB in the under-expanded case $M_j = 1.8282$ from both the models.

Considerable discrepancies are present in the over-expanded case when comparing prediction results with the experimental results. However, there is a minor improvement in over-expanded conditions for the peak SPL when compared to the Morris and Miller[13] model. One possible reason for the discrepancy between the current predictions and the experimental results in the $M_j = 1.294$ case might be the screech effects, as they modify the BBSAN spectrum.[18,42] However, the screech effects are also present in $M_j = 1.381$ case, and the peak SPL is predicted correctly. The discrepancies might have been caused due to Mach disk formation also, which occurs at the $M_j = 1.294$ case, and lowers the intensity of the shock-associated noise. Another reason for some of the discrepancy might be that the anisotropic velocities are estimated empirically, and obtaining more accurate data from DNS or LES simulations could improve the prediction results. Also, the decay of BBSAN at very high frequency does not match the experimental results. Kalyan and Karabasov[43] showed that using frequency-dependent length and time scales for the Morris and Miller[13] model considerably improves the high-frequency prediction. The same approach can be adapted to potentially improve high-frequency predictions. We have not followed their approach here because we have set out to identify the correct source term within the Navier-Stokes equations.

B. BBSAN source locations

The source locations are now evaluated based on the model. To obtain the source locations, we do not numerically integrate Eq. (34) in the spatial directions. All other operations inside the integral of Eq. (34) such as performing the DFT and integrating into wavenumber space, are performed at various Strouhal numbers. We then plot the source locations of BBSAN as contours at specific frequencies. Contour plots corresponding to fully-expanded jet Mach number $M_j = 1.611$ at two different Strouhal numbers, $St = 0.5094$ and $St = 1.0235$, are shown in Fig. 8. These Strouhal numbers correspond to the peak frequency and the first harmonic frequency for BBSAN.

At $St = 0.5094$, the source locations are roughly located between $7D$ and $9D$. Podboy[25] observed that the peak source location is between $8D$ and $15D$ for the same jet condition. Seiner and Yu[21] found that their source location is between $6D$ and $10D$ or between the 4th and 6th shock-cell for a different jet. Qualitatively, the sources from the current model for peak BBSAN are located at the end of the potential core, where the growth of large-scale instabilities is at a maximum. Also, the length scale of large-structures is approximately similar to the shock-cell spacing. This corresponds to a variety of experimental results.[18,19,21,25] We note that the source locations in the present model are correctly predicted unlike the Morris and Miller[13] model, which predicted their maximum strength as being near the nozzle exit.

For the first harmonic corresponding to $St = 1.0235$ in Fig. 8(b), the source locations have shifted upstream in the

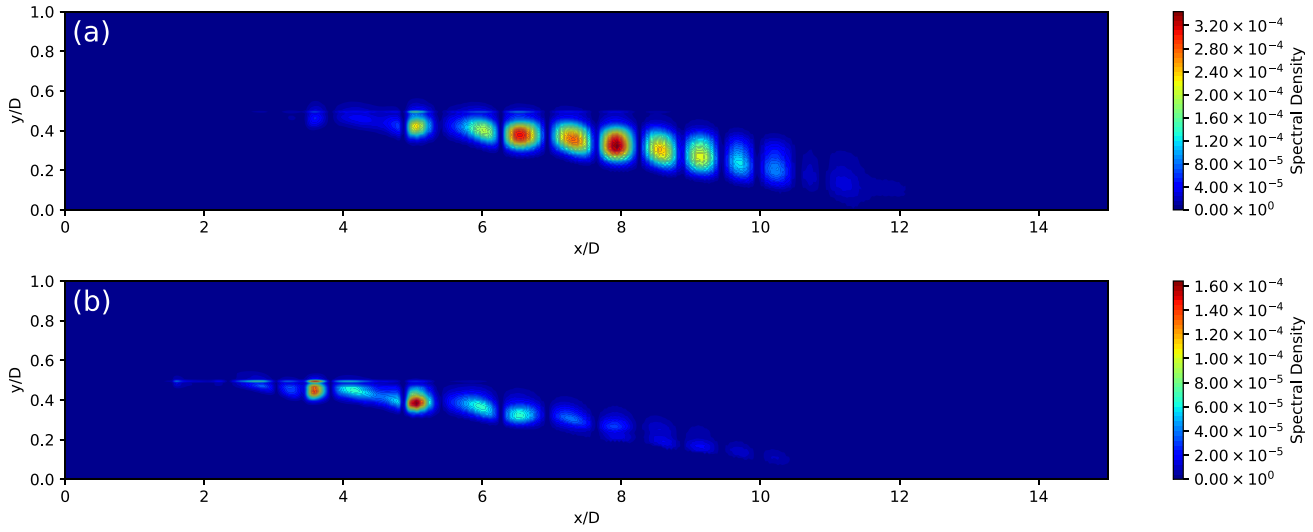

FIG. 8. (Color online) Source locations corresponding to (a) $St = 0.5094$ and (b) $St = 1.0235$ for $M_j = 1.611$.

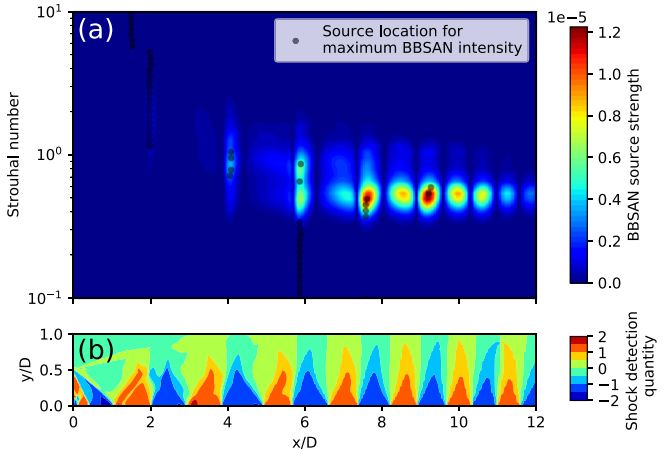

FIG. 9. (Color online) (a) BBSAN source location at different Strouhal numbers and (b) shock locations captured using a shock-capturing scheme in the jet flow-field for $M_j = 1.734$.

flow. The maximum amplitude of the sources in Fig. 8(b) is almost half when compared to the sources in Fig. 8(a). The contour plot for source strength at different axial locations for each Strouhal number corresponding to the $M_j = 1.734$ case is shown in Fig. 9(a), while the contour plot of shock locations is shown in Fig. 9(b). Following Lovely and Haimes,[44] the shock is detected from the RANS solution as $\nabla\bar{p} \cdot M_i/|\nabla\bar{p}|$. To obtain the BBSAN source strength, we integrate the source terms in the y- and z-direction at each frequency and axial location. The maximum BBSAN intensity is located at the end of the potential core at a distance between $7\,D$ and $11\,D$. The maximum intensity corresponds to the primary peak of BBSAN and is observed at the peak Strouhal number. Also, the maximum intensity at each Strouhal number is marked with a black dot in Fig. 9(a). This maximum intensity corresponds to the shock-cell locations shown in Fig. 9(b). For the higher harmonics of BBSAN, the source location gradually shifts upstream towards the nozzle. However, the intensity reduces as we move away from the peak Strouhal number. A similar trend of the source location is observed at other jet conditions. However, the dominant source locations are located near the end of the potential core.

IV. CONCLUSIONS

A model for BBSAN using an acoustic analogy approach based on the Navier-Stokes equations has been developed. The source term for BBSAN was determined by eliminating various terms using the physical mechanism of shock-noise generation. A vector Green's function is derived from the governing equations for the propagation of BBSAN, and the resultant Green's function is substituted into the convolution integral with the BBSAN source term to obtain a closed-form model for spectral density of acoustic pressure. These terms are evaluated using RANS CFD results, as well as theoretical and experimental models.

A number of empirical and semi-empirical assumptions have been made in order to identify and model the BBSAN. A model for two-point space-time cross-correlation by Ribner[34] was used to simplify the two-point cross-correlation into its magnitude and normalized correlation. The multiplication of the anisotropic velocities for scaling analysis was modeled using the turbulent kinetic energy. RANS CFD turbulence model is used for the scaling analysis as well as the arguments for the prediction model. In order to predict BBSAN, we used Gaussian functions in the normalized two-point cross-correlation for the ease of performing an analytical integration. The anisotropic velocity in the prediction model is calculated based on the Pope's composite spectra[40] and on the work of Ishihara *et al.*[41]

BBSAN predictions are performed using the newly created model, and they compare favorably with the experimental results. Source location predictions are made based on the model and it was observed that the peak noise sources are located downstream in the potential core. The source location follows some of the experimental observations that the peak noise is radiated by the interaction of weak shocks with the large-eddies in the shear layer. However, for higher harmonics of BBSAN, the peak locations shift upstream.

ACKNOWLEDGMENTS

This research was supported by the Office of Naval Research Grant No. N00014-17-1-2583. Any opinions, findings, and conclusions or recommendations expressed in this material are those of the author(s) and do not necessarily reflect the views of the Office of Naval Research.

[1]J. Doychak, "Department of Navy Jet Noise Reduction Project Overview," in *Proceedings of the 15th Annual Partners in Environmental Technology Technical Symposium and Workshop*, Washington DC (November 30–December 2, 2010).
[2]E. Mollo-Christensen, "Jet noise and shear flow instability seen from an experimenter's viewpoint," J. Appl. Mech. **34**(1), 1–7 (1967).
[3]A. Powell, "On the mechanism of choked jet noise," Proc. Phys. Soc. B. **66**(12), 1039–1056 (1953).
[4]C. K. W. Tam, "Supersonic jet noise," Ann. Rev. Fluid Mech. **27**(1), 17–43 (1995).
[5]C. Brown and J. E. Bridges, "Small Hot Jet Acoustic Rig Validation," Report No. NASA/TM-2006-214234, NASA, Washington, DC (2006).
[6]C. K. W. Tam, M. Golebiowski, and J. M. Seiner, "On the two components of turbulent mixing noise from supersonic jets," in *Proceedings of the 2nd AIAA/CEAS Aeroacoustics Conference*, 6–8 May 1996 (State College, PA, 1996), AIAA Paper No. 96-1716
[7]C.-W. Kuo, D. K. McLaughlin, P. J. Morris, and K. Viswanathan, "Effects of jet temperature on broadband shock-associated noise," AIAA J. **53**(6), 1515–1530 (2015).
[8]M. Harper-Bourne and M. J. Fisher, "The noise from shocks waves in supersonic jets," NATO AGARD-CP-131 11 (NATO, Brussels, Belgium, 1973).
[9]C. K. W. Tam, "Stochastic model theory of broadband shock associated noise from supersonic jets," J. Sound Vib. **116**(2), 265–302 (1987).
[10]C. K. W. Tam and H. K. Tanna, "Shock associated noise of supersonic jets from convergent-divergent nozzles," J. Sound Vib. **81**(3), 337–358 (1982).
[11]C. K. W. Tam and K. C. Chen, "A statistical model of turbulence in two-dimensional mixing layers," J. Fluid Mech. **92**, 303–326 (1979).
[12]C. K. W. Tam, J. A. Jackson, and J. M. Seiner, "A multiple-scales model of the shock-cell structure of imperfectly expanded supersonic jets," J. Fluid Mech. **153**, 123–149 (1985).
[13]P. J. Morris and S. A. E. Miller, "Prediction of broadband shock-associated noise using Reynolds-averaged Navier-Stokes computational fluid dynamics," AIAA J. **48**(12), 2931–2944 (2010).
[14]T. Suzuki, "Wave-packet representation of shock-cell noise for a single round jet," AIAA J. **54**(12), 3903–3917 (2016).
[15]H. K. Tanna, "An experimental study of jet noise part II: Shock associated noise," J. Sound Vib. **50**(3), 429–444 (1977).
[16]J. M. Seiner and T. D. Norum, "Experiments of shock associated noise of supersonic jets," in *Proceedings of the 12th Fluid and Plasma Dynamics Conference*, Williamsburg, VA (July 23–25, 1979), AIAA Paper No. 79-47341.

[17]J. M. Seiner and T. D. Norum, "Aerodynamic aspects of shock containing jet plumes," in *Proceedings of the 6th Aeroacoustics Conference*, Hartford, CT (June 4–6, 1980), AIAA Paper No. 80-43600.
[18]T. D. Norum and J. M. Seiner, "Location and propagation of shock associated noise from supersonic jets," in *Proceedings of the 6th Aeroacoustics Conference*, Hartford, CT (June 4–6, 1980), AIAA Paper No. 80-43599.
[19]T. D. Norum and J. M. Seiner, "Measurements of mean static pressure and far-field acoustics of shock-containing supersonic jets," Report No. NASA/TM-84521 19820025274, NASA, Washington, DC (1982).
[20]T. D. Norum and J. M. Seiner, "Broadband shock-noise from Supersonic Jets," AIAA J. **20**(1), 68–73 (1982).
[21]J. M. Seiner and J. C. Yu, "Acoustic near-field properties associated with broadband shock-noise," AIAA J. **22**(9), 1207–1215 (1984).
[22]S. A. E. Miller, "The prediction of broadband shock-associated noise using Reynolds-averaged Navier-Stokes solutions," Ph.D. thesis, The Pennsylvania State University, College Station, PA, 2009.
[23]M. Kandula, "On the scaling law for broadband shock-noise intensity in supersonic jets," in *Proceedings of the 15th AIAA/CEAS Aeroacoustics Conference*, Miami, FL (May 11–13, 2009), AIAA Paper No. 09-3318.
[24]K. Viswanathan, M. B. Alkislar, and M. J. Czech, "Characteristics of the shock-noise Component of Jet Noise," AIAA J. **48**(1), 25–46 (2010).
[25]G. G. Podboy, M. P. Wernet, M. M. Clem, and A. F. Fagan, "Noise source location and flow field measurements on supersonic jets and implications regarding broadband shock-noise," Report No. NASA-TM-2017-219544, NASA, Washington, DC (2017).
[26]D. J. Tan, D. Honnery, A. Kalyan, V. Gryazev, S. A. Karabasov, and D. Edgington-Mitchell, "Equivalent shock-associated noise source reconstruction of screeching underexpanded unheated round jets," AIAA J. **57**(3), 1200–1214 (2019).
[27]S. A. E. Miller, "Noise from isotropic turbulence," AIAA J. **55**(3), 755–773 (2017).
[28]N. Wiener, *Time Series* (MIT Press, Cambridge, MA, 1964).
[29]C. K. W. Tam and L. Auriault, "Mean flow refraction effects on sound radiated from localized sources in a jet," J. Fluid Mech. **370**, 149–174 (1998).
[30]S. A. E. Miller and P. J. Morris, "The prediction of broadband shock-associated noise including propagation effects," Int. J. Aeroacoust. **11**(7–8), 755–781 (2012).
[31]C. Henry, C. Bailly, and G. Bodard, "Statistical modeling of BBSAN including refraction effects," in *Proceedings of the 18th AIAA/CEAS Aeroacoustics Conference*, Colorado Springs, CO (June 4–6, 2012), AIAA Paper No. 2012-2163.
[32]H. E. Bass, L. C. Sutherland, A. J. Zuckerwar, D. T. Blackstock, and D. M. Hester, "Atmospheric absorption of sound: Further developments," J. Acoust. Soc. Am. **97**(1), 680–683 (1995).
[33]C. K. W. Tam and L. Auriault, "Jet mixing noise from fine-scale turbulence," AIAA J. **37**(2), 145–153 (1999).
[34]H. S. Ribner, "Theory of two-point correlations of jet noise," Report No. NASA TN D-8330, NASA, Washington, DC (1976).
[35]M. J. Lighthill, "On sound generated aerodynamically I. General theory," Proc. R. Soc. A **211**(1107), 564–587 (1952).
[36]F. R. Menter, "Two-equation eddy-viscosity turbulence models for engineering applications," AIAA J. **32**(8), 1598–1605 (1994).
[37]R. T. Biedron, J.-R. Carlson, J. M. Derlaga, P. A. Gnoffo, D. P. Hammond, W. T. Jones, B. Kleb, E. M. Lee-Rausch, E. J. Nielsen, M. A. Park, C. L. Rumsey, J. L. Thomas, K. B. Thompson, and W. A. Wood, "FUN3D Manual 13.4," Report No. NASA/TM-2018-220096, NASA, Washington, DC (2018).
[38]K. S. Abdol-Hamid, J.-R. Carlson, and C. L. Rumsey, "Verification and validation of the k-kL turbulence model in FUN3D and CFL3D codes," in *Proceedings of the 46th AIAA Fluid Dynamics Conference*, Washington, DC (June 13–17, 2016), AIAA Paper No. 2016-3941.
[39]A. N. Kolmogorov, "The local structure of turbulence in incompressible viscous fluid for very large reynolds numbers," Proc. R. Soc. A **434**(1890), 9–13 (1991).
[40]S. B. Pope, *Turbulent Flows* (Cambridge University Press, Cambridge, UK, 2000).
[41]T. Ishihara, K. Yoshida, and Y. Kaneda, "Anisotropic velocity correlation spectrum at small scales in a homogeneous turbulent shear flow," Phys. Rev. Lett. **88**(15), 154501 (2002).
[42]C. K. W. Tam, J. M. Seiner, and J. C. Yu, "Proposed relationship between broadband shock associated noise and screech tones," J. Sound Vib. **110**(2), 309–321 (1986).
[43]A. Kalyan and S. A. Karabasov, "Broadband shock associated noise predictions in axisymmetric and asymmetric jets using an improved turbulence scale model," J. Sound Vib. **394**, 392–417 (2017).
[44]D. Lovely and R. Haimes, "Shock detection from computational fluid dynamics results," in *Proceedings of the 14th Computational Fluid Dynamics Conference*, Norfolk, VA (November 1–5, 1999), AIAA Paper No. 99-3285.